Design and Control of a New Compound Double-Rotor Electric Machine for Hybrid Propulsion System

Hang Zhao, *Student Member, IEEE*, Chunhua Liu, *Senior Member, IEEE*, Zaixin Song, *Student Member, IEEE*, and Senyi Liu, *Student Member, IEEE*

***Abstract*—In this article, a new compound consequent-pole double-rotor electric machine (CCPDRM) is proposed for hybrid propulsion system application. First, the operating principle and harmonic components in CCPDRMs are elucidated. The winding factor theory for conventional permanent magnet (PM) electric machines is further extended and applied in CCPDRMs. Then, this improved theory is adopted to investigate the structure and winding scheme requirement of the proposed CCPDRMs. In addition, the control strategy for the proposed CCPDRM is established. By utilizing a parameter sweep method, the variation trends of CCPDRMs' torque density with respect to various geometrical parameters are revealed. Based on this, the structure of CCPDRMs is optimized to acquire a better electromagnetic performance. Next, the proposed CCPDRM is compared with a conventional compound bipolar double-rotor electric machine (CBDRM). It is found that the improved topology has a similar torque density but a much higher PM utilization factor and a lower PM demagnetization risk when compared with the CBDRM. Finally, a prototype is manufactured and tested in different operating modes. Furthermore, various mode-switching processes are performed to emulate the practical driving cycle of hybrid transportation. Both steady-state and dynamic mode-switching experimental results prove the effectiveness of CCPDRMs.**

***Index Terms*—Consequent pole, hybrid propulsion, mode switching, permanent magnet (PM) machine, utilization factor, winding scheme.**

I. Introduction

HYBRID propulsion systems (HPSs) inherit the advantages of both electric propulsion systems and chemical propulsion systems, so they produce less exhaust, have a better cursing capability, and are of a higher efficiency [1]. Up to now, HPSs have been successfully adopted in commercial vehicles. Although there is a trend that the automotive industry is moving toward pure electric vehicles, HPSs still have advantages when applied in heavy-duty trucks [2]. Furthermore, the HPSs have the potential to be applied in various transportations, such as aircraft and ships. Generally speaking, the service life of ships can reach up to 70 years. Due to the high manufacturing cost and long service life, it is not realistic to build a brand-new full-electric ship in some circumstances. A more feasible method is to modify the fuel-driven ship into a hybrid electric one [3], [4]. The hybrid-electric aircraft has its own benefit compared to pure electric aircraft since the aviation fuel has a much larger energy density compared to existing batteries. For aircraft that cannot be charged in the air, it is more feasible to adopt hybrid-electric structure at the current stage [5], [6]. Additionally, HPSs can be further divided into series hybrid and parallel hybrid topologies [7]. The parallel hybrid one is the emphasis of this article due to its high systematic efficiency.

The crucial component within an HPS is the continuously variable transmission (CVT), which can realize energy conversion between the internal combustion engine (ICE), batteries, and axle. The mechanical power on the axle is then utilized to drive the transportation. Among various CVTs, the electronic CVT, namely eCVT, is the most promising one, where clutches are eliminated. Fig. 1 shows the development of eCVTs, where the eCVT in the Toyota Prius is taken as an example. The Prius' eCVT is composed of two electric machines and one planetary gear, with the planetary gear serving as a power split device [8]. Recently, it has been found that magnetic-geared machines (MGMs) have the potential to replace the planetary gear in the HPS [9]. Since MGMs utilize the field-modulation effect to transmit torque and power, both the loss and vibration can be greatly reduced. Thus, the eCVT could be replaced by an MGM and a traction motor, where the traction motor is adopted to regulate the output electromagnetic torque [10]. In fact, it is proven in [11] that the MGM has a similar operating principle to a planetary gear. Later, scholars have gone a step further: some compound double-rotor electric machines (CDRMs) are proposed, in which the MGM and traction motor can be artfully integrated into one structure [12]–[14]. In these CDRMs, permanent magnets (PMs) are inserted into the modulator slots to

Manuscript received May 5, 2021; revised July 23, 2021; accepted September 5, 2021. Date of publication September 10, 2021; date of current version November 30, 2021. This work was supported in part by the Natural Science Foundation of China, China under Grants 52077186 and 51677159, in part by the Shenzhen-Hong Kong Innovation Circle Category D Project the Science Technology and Innovation Committee of Shenzhen Municipality, China under Grant SGDX2019081623101559, and in part by the Innovation and Technology Commission, Hong Kong under Project ITP/027/19AP. Recommended for publication by Associate Editor D.-C. Lee. *(Corresponding author: Chunhua Liu.)*

The authors are with the School of Energy and Environment, City University of Hong Kong, Hong Kong 999077, China, and also with the Shenzhen Research Institute, City University of Hong Kong, Shenzhen 518057, China (e-mail: zhao.hang@my.cityu.edu.hk; chualiu@eee.hku.hk; zaixin.song@my.cityu.edu.hk; senyiliu2-c@my.cityu.edu.hk).

Color versions of one or more figures in this article are available at https://doi.org/10.1109/TPEL.2021.3111815.

Digital Object Identifier 10.1109/TPEL.2021.3111815

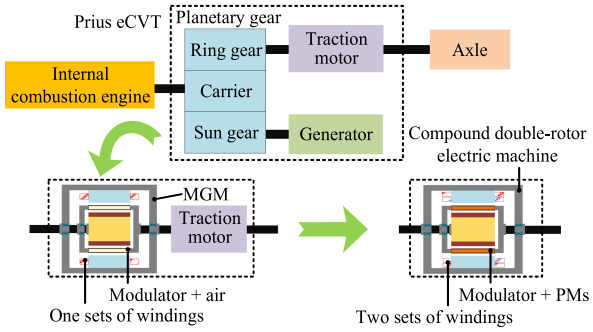

Fig. 1. Evolution of the eCVT.

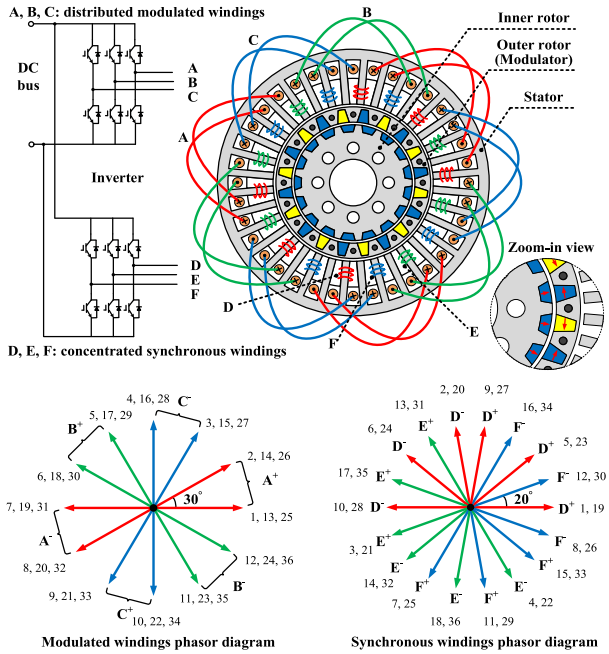

Fig. 2. Configuration and phasor diagrams of the CCPDRM.

serve as another magnetic source, and a corresponding set of windings are added on the stator to interact with this magnetic source to generate a steady torque [15], which plays the same role as a traction motor. Additionally, CDRMs can also serve as a generator to charge the batteries in the regenerative braking stage. Therefore, CDRMs are more compact, and they can be regarded as the combination of the planetary gear, traction motor, and generator in the HPS, as illustrated in Fig. 1.

A CDRM topology with integrated windings is proposed in [16]. However, only a sinusoidal pulsewidth modulation strategy is available at the current stage, and this control method reduces the voltage utilization ratio. Additionally, the insulation level of wires needs to be improved due to the rise of voltage in this scheme. A better choice is to decouple the two sets of windings within CDRMs, so a superior operating performance can be reached. To this end, a new compound consequent-pole double-rotor electric machine (CCPDRM) is proposed to replace the exiting CVT in the HPS.

The rest of this article is organized as follows. The structure requirement, operating principle, and control strategy of CCPDRMs are deduced and established based on the extended winding factor theory in Section II. In Section III, the improved CCPDRM is optimized by adopting a parameter sweep method. Then, the electromagnetic performances of the CCPDRM are evaluated and compared with its counterpart, namely the compound bipolar double-rotor electric machine (CBDRM), with respect to the torque density, PM utilization factor, and demagnetization risk. Finally, a CCPDRM prototype is manufactured and tested in both steady states and dynamic mode-switching processes within an equivalent driving cycle to verify its effectiveness.

II. Operating Principle of CCPDRMs

A. Machine Configuration

The topology and back electromotive force (EMF) phasors of studied CCPDRM are illustrated in Fig. 2, where the directions of red arrows in the zoom-in view represent the magnetization directions of PMs. The inner rotor is composed of radially magnetized consequent-pole permanent magnets (RCPMs), and the outer rotor is composed of circumferentially magnetized permanent magnets (CMPMs) sandwiched by modulator pieces. Since CCPDRMs can be regarded as the integration of two electric machines, namely a PM synchronous machine (PMSM) and an MGM, the corresponding windings of the two components are named as synchronous and modulated windings, respectively. There are two layers of coils placed on each slot of the stator: the upper layer for distributed modulated windings and the lower layer for concentrated synchronous windings. The two sets of windings are driven by two independent three-phase inverters. Hence, both the synchronous and modulated windings can be regarded as single-layer winding layouts.

Based on the operating principle of PMSMs and MGMs, the pole-pair number of synchronous and modulated windings $P_{\rm syn}$, $P_{\rm mod}$ should satisfy [17]

$$P_{\rm syn} = P_{\rm out} \quad \text{and} \quad P_{\rm mod} = Q - P_{\rm in} \tag{1}$$

where $P_{\rm in}$ and $P_{\rm out}$ are the pole-pair numbers of the RCPMs on the inner rotor and CMPMs on the outer rotor, respectively. Q is the number of modulator pieces.

Additionally, the CMPMs are inserted among the intervals of modulator pieces. Thus, its pole pair number should obey

$$P_{\rm out} = \frac{Q}{2}. \tag{2}$$

Assuming the rotating speed of inner and outer rotor are $\Omega_{\rm in}$ and $\Omega_{\rm out}$, respectively, the current frequencies in synchronous and modulated windings $f_{\rm syn}$ and $f_{\rm mod}$ should satisfy

$$f_{\rm syn} = P_{\rm out}\Omega_{\rm out}/60 \text{ and } f_{\rm mod} = (Q\Omega_{\rm out} - P_{\rm in}\Omega_{\rm in})/60. \tag{3}$$

The torque of the PMSM component is only exerted on the outer rotor, while the torque of the MGM component is exerted on both the inner and outer rotor. Thus, the torque expressions of inner and outer rotor $T_{\rm in}$ and $T_{\rm out}$ can be written as [18]

$$T_{\rm in} = -\frac{P_{\rm in}}{Q}T_{\rm mod} \quad \text{and} \quad T_{\rm out} = T_{\rm syn} + T_{\rm mod} \tag{4}$$

where $T_{\rm syn}$ and $T_{\rm mod}$ are the electromagnetic torque of PMSM and MGM components on the outer rotor. Besides, if both the synchronous and modulated windings operate simultaneously, it is named hybrid operating mode. At this moment, the electromagnetic torque value on the outer rotor is represented by $T_{\rm hybrid}$.

B. Harmonic Component Analysis

The magnetic permeance method is adopted to classify various harmonics in CCPDRMs into several categories [19].

The magnetic motive force (MMF) generated by the RCPMs on the inner rotor $F_{\rm in}(\theta, t)$ can be written in Fourier series as

$$F_{\rm in}(\theta,t)=\sum_{i=1}^{\infty}M_{{\rm RC},i}\cos iP_{\rm in}(\omega_{\rm in}t-\theta) \tag{5}$$

where $\omega_{\rm in}$ is the inner rotor's rotating speed in radian, $M_{{\rm RC},i}$ is the amplitude of *i*th harmonic in RCPMs' MMF. It should be noted that there are even-order harmonics if $\alpha \neq 0.5$.

Similarly, the air-gap permeance caused by modulator pieces $\Lambda_{\rm mod}(\theta,t)$ can be expressed in Fourier series as

$$\Lambda_{\rm mod}(\theta,t)=\Lambda_0+\sum_{j=1}^{\infty}\Lambda_{{\rm mod},j}\cos jQ\left(\omega_{\rm out}t-\theta\right) \tag{6}$$

where $\omega_{\rm out}$ is the outer rotor's rotating speed in radian, Λ_0 is the amplitude of zero-order permeance, and $\Lambda_{{\rm mod},j}$ is the amplitude of the *j*th harmonic of air-gap permeance.

Since CMPMs are fixed on the outer rotor, it rotates at the same speed as the modulator pieces. The MMF generated by CMPMs $F_{\rm out}(\theta,t)$ can be written as

$$F_{\rm out}\left(\theta,t\right)=\sum_{l=1,3,5\ldots}^{\infty}M_{{\rm CM},l}\cos lP_{\rm out}\left(\omega_{\rm out}t-\theta\right) \tag{7}$$

where $M_{{\rm CM},l}$ is the amplitude of the *l*th harmonic in CMPMs' MMF.

Thus, the radial magnetic flux density distribution on the outer air gap $B_r(\theta,t)$ can then be calculated as (8) shown at the bottom of this page.

As shown in Table I, there are three kinds of harmonics in the outer air gap, each of which rotates at a different speed: First, there is a kind of harmonics produced by the RCPMs without field modulation, which are classified as the category A. Then, a new kind of harmonics is generated when the RCPMs harmonics are modulated by the modulator pieces, and it is classified as category B. Finally, the CMPMs produce the third kind of harmonics, which is classified as category C. It should be noted that the number of modulator pieces is double the pole-pair number of the CMPMs according to (2), so the CMPMs harmonics modulated by the modulator pieces are naturally contained in category C.

TABLE I
HARMONIC COMPONENTS IN OUTER AIR GAP OF CCPDRM

Category	Harmonic order	Mechanical rotating speed	Description
A	iP_{in}	ω_{in}	RCPMs harmonics
B	$\left\|iP_{in}\pm jQ\right\|$	$\dfrac{iP_{in}\omega_{in}\pm jQ\omega_{out}}{iP_{in}\pm jQ}$	RCPMs harmonics modulated by modulator pieces
C	lP_{out}	ω_{out}	CMPMs harmonics

C. Structure Requirement Investigation

In conventional PM electric machines, the flux of one coil of the stator windings $\phi(t)$ and the corresponding induced EMF $e(t)$ are expressed, respectively, as [20]

$$\phi\left(t\right)=\Phi_f\cos\left(\omega_f t\right) \tag{9}$$

$$e\left(t\right)=-N_{\rm turn}k_{w,f}\frac{d\phi}{dt}=-N_{\rm turn}k_{w,f}\cdot 2\pi\omega_f\Phi_f\sin\left(\omega_f t\right) \tag{10}$$

where Φ_f is the amplitude of the fundamental flux, $N_{\rm turn}$ is the number of turns per phase, ω_f is the rotating speed of the fundamental flux in electric radian, and $k_{w,f}$ is the winding factor of the fundamental harmonic.

The flux and EMF expressions in (9) and (10) are feasible only when the amplitude of the fundamental harmonic is much larger than that of others, and they must be revised for CCPDRMs, where many harmonics exist. Because the flux for one coil in the stator windings is the integral of the flux density over a pole pitch area, the corresponding $\phi(t)$ and $e(t)$ in CCPDRMs are expressed in Fourier series in three categories by referring to (8)

$$\begin{aligned}\phi\left(t\right)&=\sum_{v=1}^{\infty}\Phi_v\cos\left(\omega_v t\right)\\&=\sum_{l=1,3,5\ldots}^{\infty}\Phi_{{\rm CM},l}\cos lP_{\rm out}\left(\omega_{\rm out}t\right)\\&\quad+\sum_{i=1}^{\infty}\Phi_{{\rm RC},i}\cos iP_{\rm in}\left(\omega_{\rm out}t\right)\\&\quad+\sum_{i=1}^{\infty}\sum_{j=1}^{\infty}\Phi_{{\rm mod},ij}\cos\left(iP_{\rm in}\omega_{\rm in}\pm jQ\omega_{\rm out}\right)t\end{aligned} \tag{11}$$

$$\begin{aligned}B_r\left(\theta,t\right)=F_{\rm out}\Lambda_0+F_{\rm in}\Lambda_{\rm mod}&=\underbrace{\sum_{l=1,3,5\ldots}^{\infty}M_{{\rm CM},l}\Lambda_0\cos lP_{\rm out}\left(\omega_{\rm out}t-\theta\right)}_{\text{harmonics of CMPMs}}+\underbrace{\sum_{i=1}^{\infty}M_{{\rm RC},i}\Lambda_0\cos iP_{\rm in}\left(\omega_{\rm in}t-\theta\right)}_{\text{harmonics of RCPMs}}\\&+\underbrace{\sum_{i=1}^{\infty}\sum_{j=1}^{\infty}\frac{1}{2}M_{{\rm RC},i}\Lambda_{{\rm mod},j}\cos\left[\left(iP_{\rm in}\omega_{\rm in}\pm jQ\omega_{\rm out}\right)t-\left(iP_{\rm in}\pm jQ\right)\theta\right]}_{\text{harmonics of the interaction between RCPMs and modulator}}\end{aligned} \tag{8}$$

$$e(t) = -N_{\text{turn}}\left(\sum_{l=1}^{\infty} k_{w,l}\frac{d\phi_l}{dt} + \sum_{i=1}^{\infty} k_{w,i}\frac{d\phi_i}{dt} + \sum_{i=1}^{\infty}\sum_{j=1}^{\infty} k_{w,ij}\frac{d\phi_{ij}}{dt}\right) \tag{12}$$

where $\Phi_{\text{CM},l}$, $\Phi_{\text{RC},i}$, and $\Phi_{\text{mod},ij}$ are the amplitude of the lth, ith, and $|iP_{\text{in}} \pm jQ|^{\text{th}}$ harmonic flux, respectively.

Since CCPDRMs can be regarded as the combination of an MGM and a PMSM, we can discuss their powers and torque compositions separately. Take the synchronous winding, for instance, the current in stator windings is assumed as

$$i_{\text{syn}}(t) = I_{\text{syn}} \sin\left(P_{\text{out}}\omega_{\text{out}}t\right) \tag{13}$$

where I_{syn} is the amplitude of the current in synchronous windings. Then, the instantaneous power of the synchronous windings $p_{\text{syn}}(t)$ at the moment t can be written as (14) shown at the bottom of this page.

The integral of the first part in (14) equals zero for every mechanical period due to the orthogonal characteristic of trigonometric functions [21]. For the second part, its integral is not zero. Hence, the second part in (14) can produce effective torque, while the first part is related to torque ripple. For an electric machine, we wish the effective torque to be as large as possible while the torque ripple to be as small as possible. In other words, the useful winding factor $k_{\text{syn},P_{\text{out}}}$ should be large while other nonrelated winding factors should be small. Similarly, the fundamental harmonic order for modulated windings is (Q-P_{in})th, namely (P_{mod})th, and its useful winding factor $k_{\text{mod},(Q-P_{\text{in}})}$ should be as large as possible, while the others should be small.

The windings actually serve as a comb filter that only specific spatial harmonics can pass and generate EMF, while other harmonics are attenuated [17]. The winding factor k_w can be regarded as the transfer function of the "winding filter," and its value is in the range of [0, 1]. Although there are plenty of harmonics in CCPDRMs, nonrelated harmonics will be eliminated by the winding scheme as if they were not existing. For the eliminated harmonics, their winding factor values are zero. The harmonics generation and elimination process from the PM sources to the stator windings are depicted in Fig. 3. Once the nonrelated harmonics are cut down or eliminated, the total harmonic distortion (THD) of the induced EMF can be minimal, leading to a low torque ripple.

D. Winding Scheme Determination

To further verify the "winding filter," winding factors of synchronous windings and modulated windings for those main

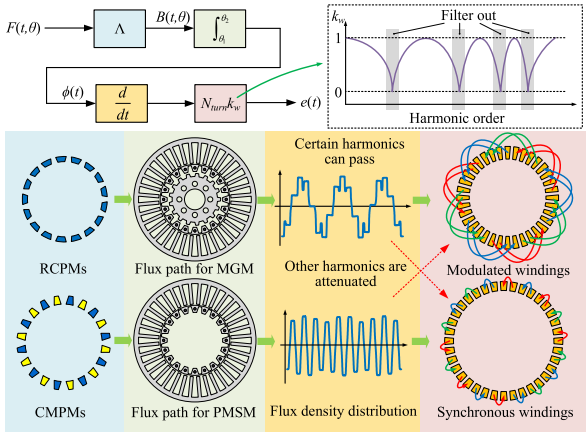

Fig. 3. Illustration of harmonics generation and elimination.

TABLE II
WINDING FACTORS OF MAIN HARMONICS IN CCPDRMS

Harmonic order	Category	The winding factor for synchronous windings	Winding factor for modulated windings
3	B	0	0.966
10	C	0.647	0
17	A	0	0
20	C	0.442	0
23	B	0	0

harmonics existing in the outer air gap of CCPDRM are calculated by the EMF phasor method [22], [23]. The EMF phasor of the coil side i for the nth spatial harmonic is given by

$$\vec{E}_{i,n} = \text{sign}(S(i))e^{j\frac{2\pi n}{Z}|S(i)|} \tag{15}$$

where S is the winding connection vector for a single phase, and $S(i)$ is the ith element of vector S.

In this article, $P_{\text{in}} = 17$, $P_{\text{out}} = 10$, $Q = 20$, $P_{\text{mod}} = 3$, and $P_{\text{syn}} = 10$. Therefore, the winding connection vector S_A of phase A that belongs to the modulated windings and S_D of phase D that belongs to the synchronous windings can be expressed as

$$S_A = \left[1\ 2\ -7\ -8\ 13\ 14\ -19\ -20\ 25\ 26\ 31\ 32\right] \tag{16}$$

$$S_D = \left[1\ -2\ 5\ -6\ 9\ -10\ 19\ -20\ 23\ -24\ 27\ -28\right]. \tag{17}$$

Then, the winding factor k_n for the nth harmonic is written as

$$k_n = \frac{1}{Z/3}\left|\sum_{i=1}^{Z/3}\vec{E}_{i,n}\right|. \tag{18}$$

The winding factors of the prominent harmonics in the CCPDRMs are provided in Table II. It can be observed that the synchronous winding layout can effectively eliminate harmonics

$$p_{\text{syn}}(t) = \underbrace{\left[-2\pi N_{\text{turn}}\sum\nolimits_{v=1,2,3\ldots\&v\neq P_{out}}^{\infty} k_{\text{syn},v}\omega_v\Phi_v I_{\text{syn}}\sin\left(\omega_v t\right)\sin\left(P_{\text{out}}\omega_{\text{out}}t\right)\right]}_{\text{noneffective}} + \underbrace{\left[-2\pi N_{\text{turn}}k_{\text{syn},P_{\text{out}}}P_{\text{out}}\omega_{\text{out}}\Phi_{\text{CM},1}I_{\text{syn}}\sin(P_{\text{out}}\omega_{\text{out}}t)\sin\left(P_{\text{out}}\omega_{\text{out}}t\right)\right]}_{\text{effective}} \tag{14}$$

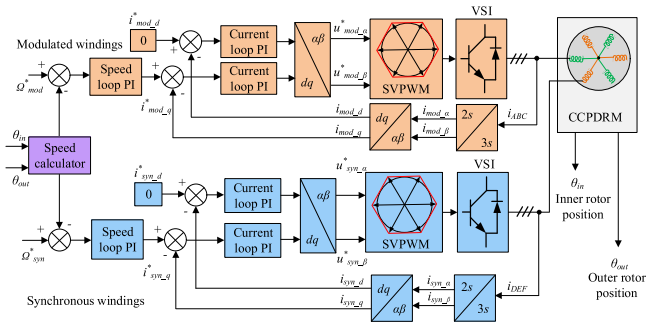

Fig. 4. Control diagram of the proposed CCPDRM.

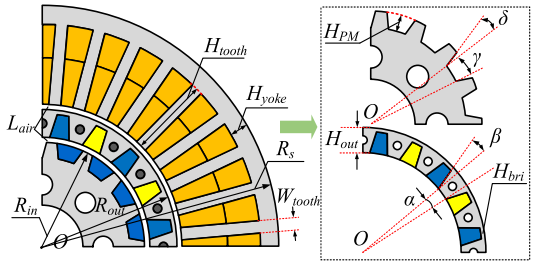

Fig. 5. Geometrical parameters in CCPDRMs to be determined.

from categories A and B and modulated winding layout can effectively eliminate the harmonics from categories A and C. Hence, the two electric machine components within CCPDRMs can work independently without influencing each other. In other words, they are magnetically and electrically decoupled from each other. Then, if the proposed CCPDRMs are further applied in HPSs, the HPS can exhibit good performances in various operating modes.

E. Control Strategy

Once the synchronous and modulated windings are decoupled, the two machine components can be controlled independently. The control of MGM component can be equivalent to a conventional PMSM, and the only difference is that its virtual *d* axis is determined by both inner and outer rotor positions [15]. Then, as illustrated in Fig. 4, the field-oriented control strategy is applied for both PMSM and MGM components, which magnetic field rotating speeds can be determined by (3).

It should be noted that the outer rotor is under the force of both PMSM and MGM components, and the force of each component is regarded as interference from the other. Therefore, the PI parameters of the speed and current loops of the two machine components should be considered globally. For instance, the PI parameters in different operating modes, such as the steady and dynamic states, should be designed separately to reach a better performance.

Additionally, different from single-rotor motors, the output torque of CCPDRM is determined by the currents in the two electric machine components. So, there can be infinite current combinations for a given output torque value. A torque distribution method was proposed in [24], where the current reference values are provided via calculation. However, this method eliminates the speed loop, which might decrease the machine's dynamic performance. Hence, in this article, the speed loop is not removed. Instead, the torque distribution between the PMSM and MGM components is realized by setting a *q*-axis current amplitude limitation to one electric machine component. And then the current of the other component can be determined uniquely. Thus, the torque and power distribution in different proportions between the PMSM and MGM components can be realized in dynamic and steady states.

III. Geometrical Parameters Determination

There are two significant indexes for propulsion motors, namely the volumetric torque density and PM volumetric torque density. Since the proposed CCPDRMs are the synthesis of two separate motor components, we should consider the two indexes for the two motor components simultaneously concerning the variations of geometrical parameters in CCPDRMs.

Since the size of the CCPDRM is predetermined at the initial stage, the variation trends of output torque $T_{\rm syn}$ and $T_{\rm mod}$ in the PMSM and MGM components are used to represent the corresponding volumetric torque density. As for PM volumetric torque density, they are defined as

$$\tau_{\rm syn} = \frac{T_{\rm syn}}{V_{\rm CMPM}} \quad \text{and} \quad \tau_{\rm mod} = \frac{T_{\rm mod}}{V_{\rm RCPM}} \tag{19}$$

where $\tau_{\rm syn}$ and $\tau_{\rm mod}$ are the PM volumetric torque density for PMSM and MGM components, respectively. $V_{\rm CMPM}$ and $V_{\rm RCPM}$ are the volume of CMPMs on the inner rotor and the volume of RCPMs on the outer rotor, respectively.

The main geometrical parameters in the CCPDRM are illustrated in Fig. 5. There are more than ten variables in the topology, and the magnetic flux density distribution is complicated due to the existence of two different PM sources. For the time-saving purpose, these variables are optimized to acquire a large torque density with respect to the total volume and PM volume subsequently by adopting a parameter sweep method in the finite-element analysis (FEA) software. Within the CCODRM, some parameters are highly related with respect to the torque of modulated and synchronous windings. The design obtained by using single-variable parameterization may not be the optimal one [25], and the highly related parameters should participate in the process of parameter sweep simultaneously. To this end, two variables are selected for a combined parameter sweep study with respect to the CCPDRM.

A. Inner and Outer Rotor Radius Optimization

The amplitude of the output torque of a motor has a linear relation with the square of the air-gap radius. Besides, the air-gap radius further affects the stator winding area and the number of turns of coils. Therefore, the radii of the inner and outer air gap in the CCPDRM should be settled down at the first stage. The inner rotor's outer radius $R_{\rm in}$ and the thickness of outer rotor $H_{\rm out}$ are used as the independent variables to represent the variations of inner and outer air-gap radii. The variations between volumetric torque density, PM volumetric torque density, and $R_{\rm in}$, $H_{\rm out}$ are

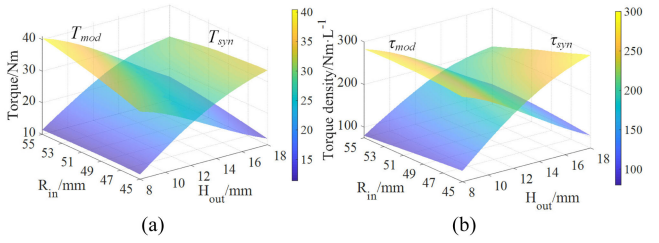

Fig. 6. Variation relations. (a) T_{mod}, T_{syn} and R_{in}, H_{out}. (b) τ_{mod}, τ_{syn} and R_{in}, H_{out}.

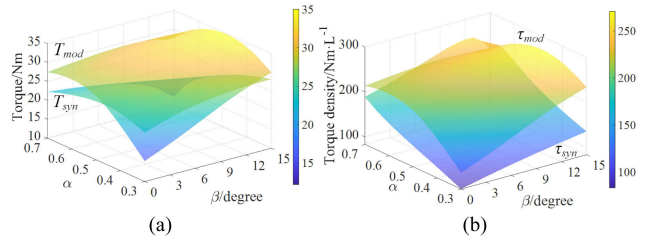

Fig. 7. Variation relations. (a) T_{mod}, T_{syn} and α, β. (b) τ_{mod}, τ_{syn} and α, β.

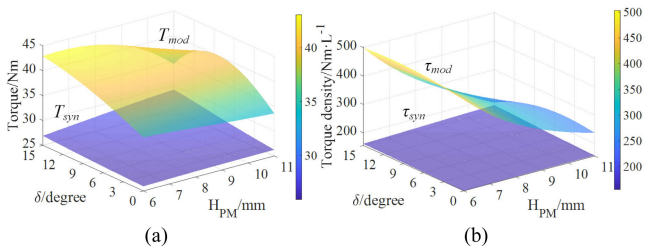

Fig. 8. Variation relations. (a) T_{mod}, T_{syn} and δ, H_{PM}. (b) τ_{mod}, τ_{syn} and δ, H_{PM}.

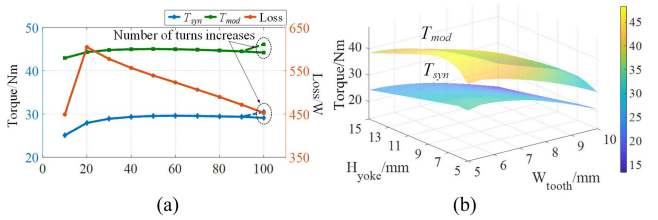

Fig. 9. Variation relations. (a) T_{mod}, T_{syn}, total loss, and slot opening ratio. (b) T_{mod}, T_{syn} and H_{yoke}, W_{tooth}.

depicted in Fig. 6. It can be observed that the general variation trends of τ_{syn} and τ_{mod} are in coincidence with that of T_{syn} and T_{mod}, except for the boundary regions due to local magnetic saturation. What is more, the variation trend of T_{mod} and T_{syn} are in opposition to each other. In other words, one cannot maximize T_{mod} and T_{syn} simultaneously, and a tradeoff must be made. To this end, the values of R_{in} and H_{out} are selected as 50.5 and 13.0 mm, respectively, for further optimization.

B. Outer Rotor Parameter Optimization

The modulator pieces serve as the flux paths for both MGM and PMSM components. Inspired by [26], a slant angle β is assigned to the CMPMs on the outer rotor during optimization. Since the CMPMs and modulator pieces are geometrically complementary, the arc ratio of modulator pieces α can affect the torque density of both MGM and PMSM components. The variation relations between torque density, PM torque density, and α, β are depicted in Fig. 7. It can be seen that for torque and PM utilization factor of the MGM component, their maximum values occur when α equals 0.5, which means that the arc angle of modulator pieces and CMPMs are divided equally. The torque of the PMSM component decreases rapidly with the increase of α, although its PM utilization factor increases at the same time. To take account of the value of T_{syn}, we select the values of α and β as 0.40° and 15.0° in this article.

C. Inner Rotor Parameter Optimization

Similar to the trapezoidal shape of the CMPMs, a slant angle δ is also assigned to the RCPMs on the inner rotor during optimization. Additionally, the thickness of CMPMs H_{PM} is also taken into account during optimization. The variation relations between torque density, PM torque density, and δ, H_{PM} are depicted in Fig. 8. It can be observed that for the value of H_{PM} below 8 mm, with the increase of δ, the torque of the MGM component increases. However, its PM torque density decreases rapidly as H_{PM} increases. As for the torque of the PMSM component, its value varies a little with the change of δ and H_{PM} since the inner rotor has little influence on the PMSM component's flux path. Therefore, the values of δ and H_{PM} are selected as 15.0° and 5.5 mm in this article.

D. Stator Parameter Optimization

For fractional-slot PMSM, the open-slot structure may cause a high-frequency magnetic field component, increasing the loss [27]. There are naturally two kinds of harmonics within CCP-DRMs, so the influence of slot opening width on the performance of CCPDRMs needs to be studied in detail. Fig. 9(a) illustrates the variation trends of T_{syn}, T_{mod}, and the total loss (including iron loss, copper loss, and PM eddy current loss) with respect to the slot opening width. With the increase of slot opening, T_{syn}, T_{mod} first increase, then decrease, and the total loss decreases. If the open-slot structure is adopted, not only the slot filling area for wires further increases, a pre-forming of the stator coils, which simplifies the assembly process, can also be possible. Therefore, an open-slot structure is adopted for the proposed CCPDRMs.

For the stator yoke thickness H_{yoke} and the stator tooth width W_{tooth} optimization, the total PM volume does not change, so only the volumetric torque density T_{syn} and T_{mod} are considered. Fig. 9(b) illustrates the variation relations between T_{syn}, T_{mod}, and H_{yoke}, W_{tooth}. It can be seen that with the increase of W_{tooth}, both T_{syn}, T_{mod} decrease due to the reduction of turns of coils. However, with the increase of H_{yoke}, T_{syn} and T_{mod} increase first and decrease later, which is caused by severe magnetic saturation in the stator back yoke region. To maximize the output torque, we choose the values of H_{yoke} and W_{tooth} as 8.5 and 5.5 mm in this article.

TABLE III
OPTIMIZED PARAMETERS OF THE CCPDRM AND CBDRM

	Symbol	CBDRM	CCPDRM
Stator outer radius/mm	R_s	110.0	
Axial length/mm	L	100.0	
Iron bridge thickness/mm	H_{bri}	2.0	
Inner rotor outer radius/mm	R_{in}	52.1	50.5
Outer rotor thickness/mm	H_{out}	14.7	13.0
Arc ratio of modulator piece	α	4.0×10^{-1}	4.1×10^{-1}
Slant angle of CMPMs/degree	β	14.7	15.0
Inner rotor PMs thickness/mm	H_{PM}	5.0	5.5
Stator tooth width/mm	W_{tooth}	5.8	5.5
Stator back iron thickness/mm	H_{yoke}	8.3	8.5
Number of turns in synchronous windings	N_{syn}	21	23
Number of turns in modulated windings	N_{mod}	21	23
Current density/A·mm^{-2}	D	5.0	

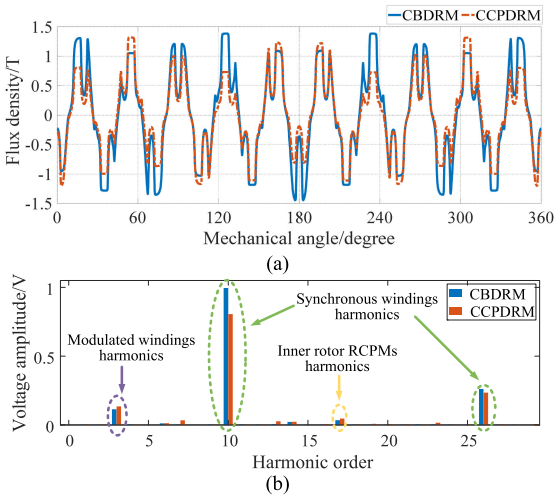

Fig. 10. Radial component magnetic flux density of the outer air gap on no-load condition for the CBDRM and CCPDRM. (a) Radial component magnetic flux density distribution. (b) Corresponding FFT distribution.

IV. PERFORMANCE COMPARISON AND EVALUATION

To further reveal the improvement of the PM utilization factor of the proposed CCPDRMs over CBDRMs, the electromagnetic performances of these two types of machines are compared. Both two machines are optimized independently, and the corresponding optimized geometrical parameters are listed in Table III. It should be noted that for a fair comparison purpose, the size, air-gap length, and filling factor of the two machines are set equal. Additionally, the silicon steel material 50WW250 is adopted for both machines.

A. No-Load Performance

The radial-component magnetic flux density on the outer air gap at the no-load condition and the corresponding fast Fourier transform (FFT) spectrum for both the CCPDRM and CBDRM are depicted in Fig. 10. The working harmonics for the synchronous windings are 10th and 26th, while the working harmonics for the modulated windings are 3rd. It should be noted that the 26th harmonic is generated by the interaction between the outer rotor's CMPMs and the stator teeth. Additionally, the harmonic amplitude of the inner rotor's RCPMs is relatively small on the outer air gap. It proves that the modulator pieces are magnetically saturated. Comparing the corresponding harmonic amplitudes between CCPDRM and CBDRM, the amplitudes of synchronous winding harmonics in the CBDRM are more significant than that of the CCPDRM due to its thicker outer rotor structure. In contrast, the amplitudes of modulated windings' harmonics in the CBDRM are smaller than that of the CCPDRM.

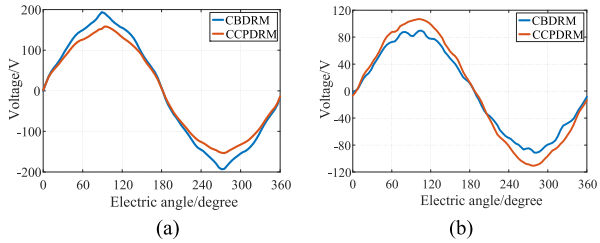

Fig. 11. Back EMF waveforms of the CBDRM and CCPDRM. (a) Synchronous windings. (b) Modulated windings.

TABLE IV
ON-LOAD PERFORMANCE COMPARISONS BETWEEN CCPDRM AND CBDRM

Items	CBDRM	CCPDRM
T_{syn}/Nm	33.1	30.4
T_{mod}/Nm	37.8	46.3
T_{hybrid}/Nm	70.6	73.8
τ_{syn}/Nm·L^{-1}	176.5	181.1
τ_{mod}/Nm·L^{-1}	247.5	480.0
Total PM amount/L	3.4×10-1	2.6×10-1
Iron loss/W	453.2	389.3
PM eddy current loss/W	35.7	23.9
Copper loss/W	554.7	607.5
Efficiency/%	91.4	91.9

The back EMF waveforms of the PMSM and MGM components in CCPDRM and CBDRM are depicted in Fig. 11. It can be observed that for both the CCPDRM and CBDRM, the THDs of their back EMFs are small, proving that the PMSM and MGM components can work independently. Additionally, the modulated windings' back EMF of the CCPDRM has an even smaller THD than that of the CBDRM due to the higher degrees of freedom concerning inner rotor PMs geometrical parameter optimization.

B. On-Load Performance

The on-load rated electromagnetic performance data for both the CBDRM and CCPDRM are provided in Table IV. For the MGM component, the PM volumetric torque density of CCPDRM is 1.94 times of that of the CBDRM; as for the PMSM component, the corresponding PM volumetric torque density of the two topologies are similar. Additionally, the efficiency of the CCPDRM is higher than that of the CBDRM. Besides, for the CCPDRM, its hybrid torque is less than the torque sum of the PMSM and MGM components, while for the CBDRM, its hybrid torque almost equals to the torque sum of the PMSM and MGM components. This phenomenon indicates that the magnetic saturation effect is more serious in CCPDRMs due to the larger magnetic permeance in the flux path.

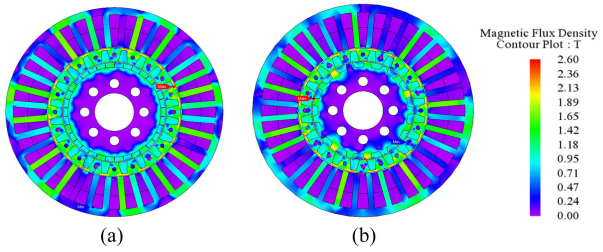

Fig. 12. On-load magnetic flux density map. (a) CBDRM. (b) CCPDRM.

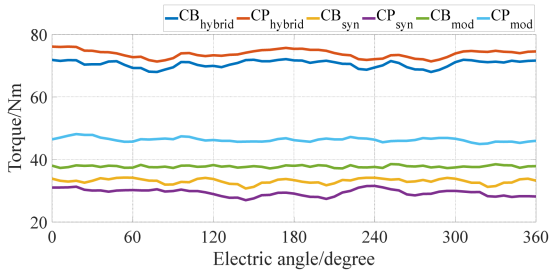

Fig. 13. Torques of CBDRM and CCPDRM within one electric period.

The on-load magnetic flux density maps of the CCPDRM and CBDRM are depicted in Fig. 12, where "CB" refers to the CBDRM, and "CP" refers to the CCPDRM. It can be observed that the rotor iron part adjacent to RCPMs of CCPDRM is highly saturated to form a closed flux path. This is why the PM volumetric torque density of the CCPDRM is almost double that of the CBDRM. The on-load torque waveforms of the CBDRM and CCPDRM with different windings electrified are depicted in Fig. 13. It can be observed that the torque ripple for synchronous windings working alone is larger than that of modulated windings. Hence, the torque ripple on hybrid mode mainly originates from the PMSM component.

C. Demagnetization Consideration

Another concern is whether the PMs in CCPDRMs will suffer from the demagnetization risk while working at the rated operating mode. The rated operating temperature for motors in the HPS is assumed as 120 °C [28]. The PM material for the two machines is selected as N35SH, whose demagnetization flux density is 0.26 T at 120 °C. For the PMs within electric machines, the corner regions are the most vulnerable and of the highest demagnetization risk. This phenomenon can be observed for the on-load flux density distribution depicted in Fig. 12. Considering structural symmetry, three points at the corners of inner rotor PMs' outer surface and outer rotors PMs' inner surface are selected as the observation points for PMs' demagnetization risk analysis, as can be seen in Fig. 14 (a) and (b). The magnetic flux density variations on the selected points over the 360-degree mechanical angle at rated current density and temperature are depicted in Fig. 14(c). Unlike single-rotor electric machines, the periodic pattern of double-rotor machines is determined by both inner and outer rotors [29]. However, the purpose of this section is to evaluate the demagnetization risk of two types of double-rotor machines, namely the CBDRM and CCPDRM, and

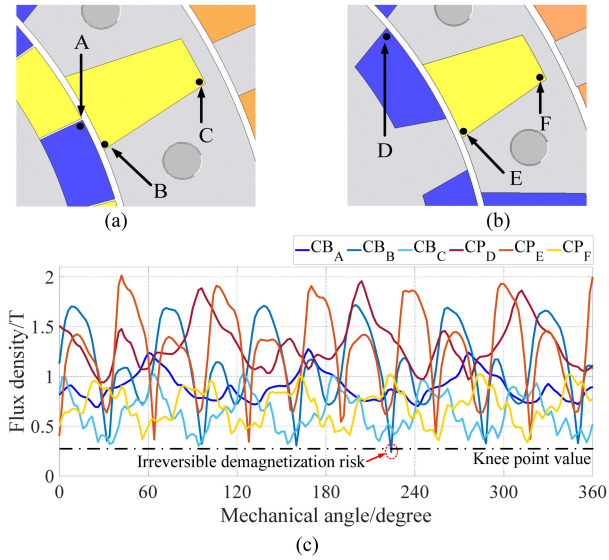

Fig. 14. Demagnetization analysis. (a) Points selection of CBDRM. (b) Points selection of CCPDRM. (c) Magnetic flux density over one electric period.

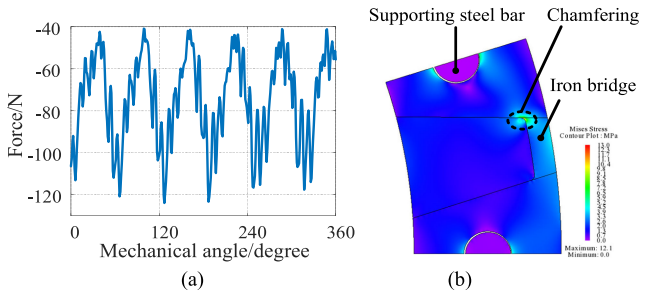

Fig. 15. Iron bridge mechanical analysis. (a) Radial magnetic force on rated condition. (b) von Mises stress distribution.

it is enough to use the data within a 360° mechanical angle for evaluation. It can be found that the minimum flux density occurs on point B for the CBDRM and point E for the CCPDRM. This indicates that the inner surface of CMPMs is the most vulnerable region that suffers from demagnetization risk. The minimum flux density of point B over 360° mechanical angle is below the knee point, while that of point E is above the knee point, which is represented as the dot-dash line in Fig. 14(c). It proves that the CCPDRM has a lower demagnetization risk compared to the CBDRM. Therefore, a higher model number PM material should be adopted in the CBDRM to reduce PM demagnetization risk from happening, which increases manufacturing cost.

D. Mechanical Strength Consideration

The iron bridge on the outer rotor must withstand not only the centrifugal force from the PMs on the inner rotor but also the magnetic force from the outer air gap. Hence, it is the flimsiest part of the CDRMs. The iron bridge thickness is set the same for both the CBDRM and CCPDRM, and the maximum electromagnetic torque values on the outer rotor are similar. Hence, it is enough to use the CCPDRM as a representative for the mechanical strength examination. Fig. 15(a) shows the

magnetic force that the iron bridge withstands on the hybrid operating mode. Both the synchronous and modulated windings are electrified with the rated currents, where the direction away from the center is regarded as the positive direction of the force. Then, the magnetic force is mapped to mechanical analysis for the outer rotor. Fig 15(b) shows the von Mises stress distribution considering the magnetic force and centrifugal force. The maximum von Mises stress of the outer rotor is 13 MPa, far lower than the yield limit of the silicon steel 50WW250 used in the CCPDRM, namely 405 MPa [30]. Since the lower limit of the thickness of iron bridge H_{bri} is set very conservatively during optimization, the maximum von Mises stress can be much lower than the yield limit of the material. Actually, H_{bri} can be further decreased to reach better electromagnetic performance in practical application. Additionally, the maximum Mises stress occurs on the interface between the modulator piece and the iron bridge, where the corner must be chamfered to reduce the stress in case of breakage.

V. Experimental Validation

A. Prototype Machine

A CCPDRM prototype is manufactured based on the optimized parameters in Table III. The explosive view, components, and the corresponding test bench of the prototype are depicted in Fig. 16. The supporting steel bars on the outer rotor are inserted on the holes at the center of each modulator piece to fix the laminated silicon steel to prevent axial skew and reinforce mechanical strength, which is a typical mechanical structure of the modulator [31], [32]. The rotor covers are added to the front and back ends of the outer rotor to improve the mechanical strength. Additionally, both the inner rotor and outer rotor are fixed at the front and back via four bearings on the rotor covers and end caps to prevent eccentricity, as shown in Fig. 16(a). As mentioned in Section II-E, the proposed CCPDRM can be driven by adopting a field-oriented control strategy on synchronous and modulated windings independently since its two sets of windings are decoupled. The rotating speed of modulated windings' magnetic field is determined by using (3), where the angular position information of inner and outer rotor is acquired by the encoders on their shafts.

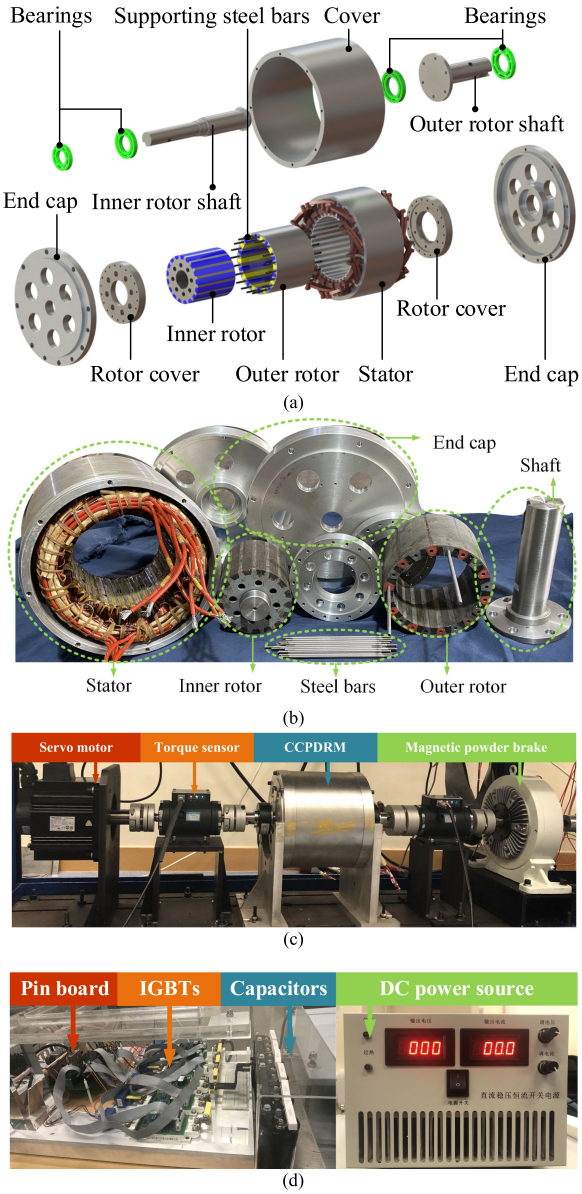

Fig. 16. Prototype CCPDRM. (a) Exploded view drawing. (b) Machine components. (c) Test bench. (d) Motor drive hardware.

B. No-Load Test

The no-load performance of the CCPDRM is tested when its inner rotor is locked by a magnetic powder brake, with its outer rotor being driven by a servo motor rotating at 1000 r/min. The back EMFs compared with FEA are given in Fig. 17. It can be observed that the amplitude of the fundamental harmonic in the measured EMF is about 95% of that of FEA. The error could be caused by the overestimated silicon lamination factor and ignorance of the end effect in a two-dimensional FEA simulation.

Besides, there is a tradeoff between the modulated windings and synchronous windings on the electromagnetic torque and the THD. From the optimization in Section III, it can be observed that the electromagnetic torque of modulated windings is larger than that of the synchronous windings. Additionally, the THDs of measured back EMFs of synchronous and modulated windings are 4.1% and 3.0%, respectively. It should be noted that the back EMF THD for the proposed CCPDRM is very low compared to existing double-rotor electric machines [9], [11], [16], so its torque ripple in on-load operation will be smaller, too.

C. On-Load Test

Fig. 18 gives the inner and outer rotors' torque amplitude comparisons of the prototype and FEA results in different operating modes with different current densities. It can be observed that the tested inner and outer rotor's torques are a bit smaller than that of FEA due to many practical factors, including lower silicon lamination factor, larger iron loss caused by pulse width modulation

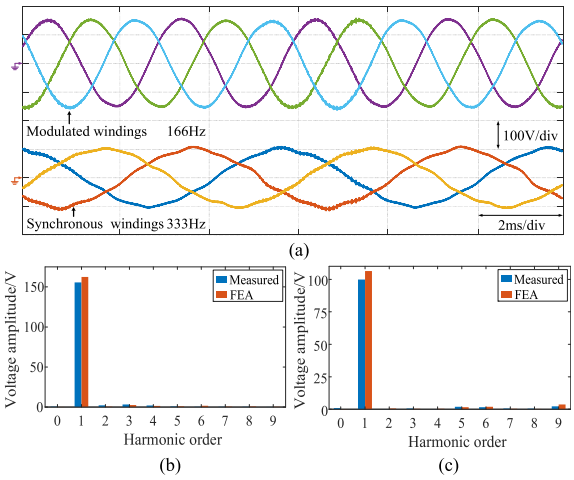

Fig. 17. No-load test. (a) Back EMF waveforms of synchronous and modulated windings. (b) EMF harmonic amplitude comparisons for synchronous windings. (c) EMF harmonic amplitude comparisons for modulated windings.

harmonics, end effect, and uncounted stray loss. Additionally, when the synchronous windings work alone, the electromagnetic torque on the inner rotor is about zero, indicating that the two sets of windings can work independently without influencing each other.

For the CCPDRM applied in the HPS, if the synchronous windings works alone, the output power comes from the batteries only. In this mode, the rotating speed of the outer rotor is the lowest. If the modulated windings works alone, the output power mainly comes from ICE. If both the modulated windings and synchronous windings work together, the output power reaches its maximum. In this hybrid mode, the output power comes from both the batteries and ICE. The waveforms of typical on-load currents and the rotating speed of the outer rotor in different working modes are depicted in Fig. 19. It can be observed that the rotating speed can be kept at a constant in different modes. Besides, the synchronous windings and modulated windings would not influence each other if they work simultaneously, and the current waveforms can maintain sinusoidal shapes.

As for the torque ripple, the tested and simulated torque ripples in Fig. 19(a) are 10.5% and 13.5%, respectively. The tested and simulated torque ripples in Fig. 19(b) are 12.6% and 7.5%, respectively. The tested and simulated torque ripples in Fig. 19(c) are 12.9% and 7.8%, respectively. It should be noted that the torque ripples in the latter two operating conditions, where the modulated windings join in the operation, are more significant than those in the simulated results. The larger torque ripple in the experiment is caused by the sight eccentricity issue, which cannot be absolutely eliminated in double-rotor electric machines.

D. Dynamic Test

As mentioned in Section I, the application of HPSs is not limited to vehicles, and it can be extended to ships and aircraft. The application of HPSs in hybrid-electric vehicles is taken as an instance for the study of dynamic performance here. Based on the standard New European Drive Cycle (NEDC) [33], the driving speed range is divided into three sections corresponding to different operating modes of the proposed HPS, as illustrated in Fig. 20. The speed range of 0–35 km/h corresponds to the operating mode where the synchronous windings works alone; the speed range of 35–85 km/h corresponds to the operating mode where the modulated windings works alone; the speed range of 85–120 km/h corresponds to the operating mode where both windings work, namely hybrid mode.

After that, the NEDC is matched to the equivalent experimental driving cycle of the CCPDRM prototype shown in Fig. 21: the synchronous windings operates alone within the speed range of 200–300 r/min; the modulated windings operates alone within the speed range of 300–500 r/min; both windings operate within the speed range of 500–600 r/min. Due to the power limitation in the laboratory, the maximum rotating speed of the outer rotor within the CCPDRM is set as 600 r/min, and the rotating speed of the inner rotor is fixed as 200 r/min to simulate that the ICE operates at its highest efficiency point.

The experimentally equivalent driving cycle is arranged as follows: First, the vehicle startup from zero speed, and the synchronous windings operates to output power. Then, as the driving speed increases, the propulsion system should switch from the synchronous windings' operation to the modulated windings' operation. In this mode, both the modulated windings and ICE output power to drive the vehicle. Next, the vehicle continues to accelerate. When it reaches a critical speed value that the modulated windings output its maximum power, the synchronous windings participate, and the propulsion system works in hybrid operating mode. When the vehicle decelerates, the modulated windings quits operation first, and the synchronous windings operates to charge the batteries.

Additionally, in Fig. 21, "*mod* winding" and "*syn* winding" refer to the modulated windings and synchronous windings, respectively. The red arrow represents that the component outputs power, while the blue arrow represents that the component absorbs power to charge the batteries. It should be noted that the synchronous and modulated windings can absorb power to charge the batteries, and the ICE can only output power to drive the vehicle.

For the mode switching between the synchronous and modulated windings, a transition process should be added. For instance, the modulated windings should join in first, and then the synchronous windings can quit operation once the rotating speed of the outer rotor becomes stable. If the modulated windings quits operation and the synchronous windings join simultaneously, a significant rotating speed decrease will be observed, which is extremely dangerous in practical operation.

Since both the modulated and synchronous windings exert electromagnetic torques on the outer rotor. The nonoperating windings should be blocked in a specific operating mode; otherwise, it will feedback the electricity to the direct-current (dc) bus. Thus, the enabling signals are assigned to the IGBTs belonging to both synchronous and modulated windings to make them connected or disconnected to the dc bus. For instance, in a pure electric mode where the synchronous windings operate alone, the modulated windings should be disconnected from the dc bus.

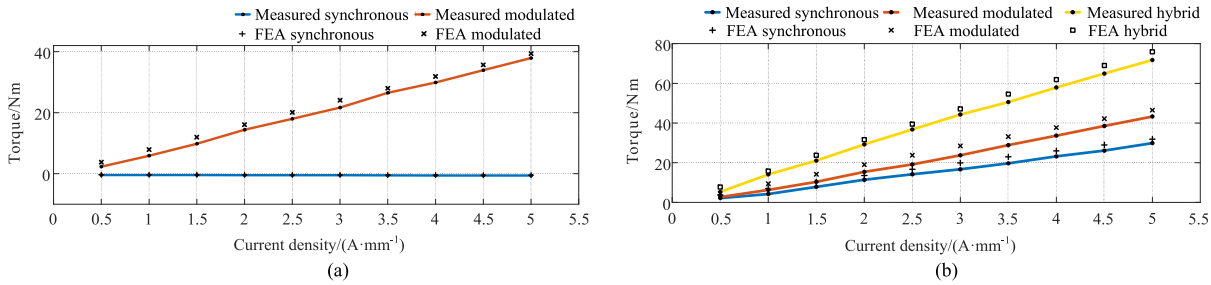

Fig. 18. Average torque of different operating modes with different current densities. (a) Inner rotor. (b) Outer rotor.

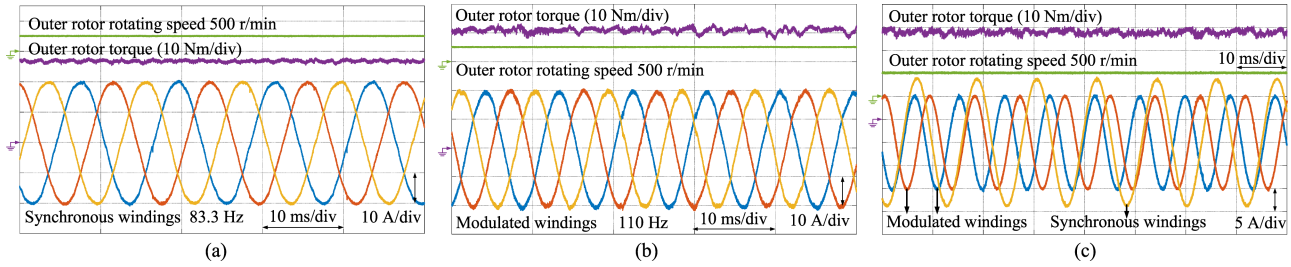

Fig. 19. Steady-state currents and rotating speeds. (a) Synchronous windings alone. (b) Modulated windings alone. (c) Both synchronous and modulated windings.

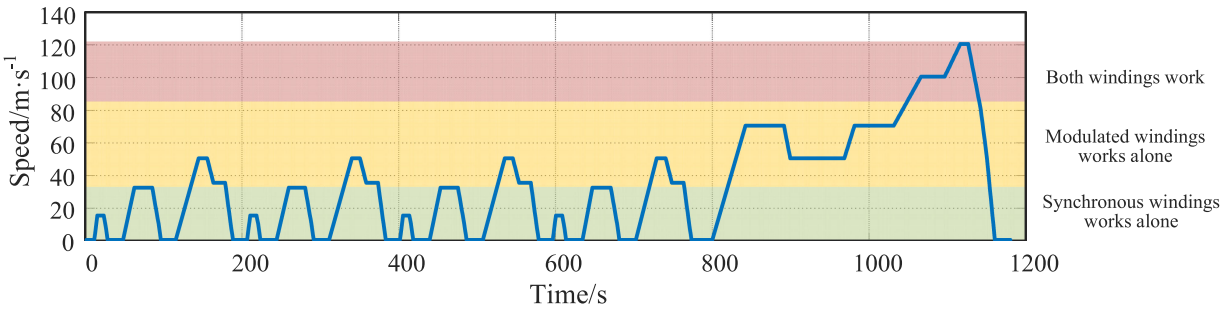

Fig. 20. Matching of the proposed HPS in the NEDC.

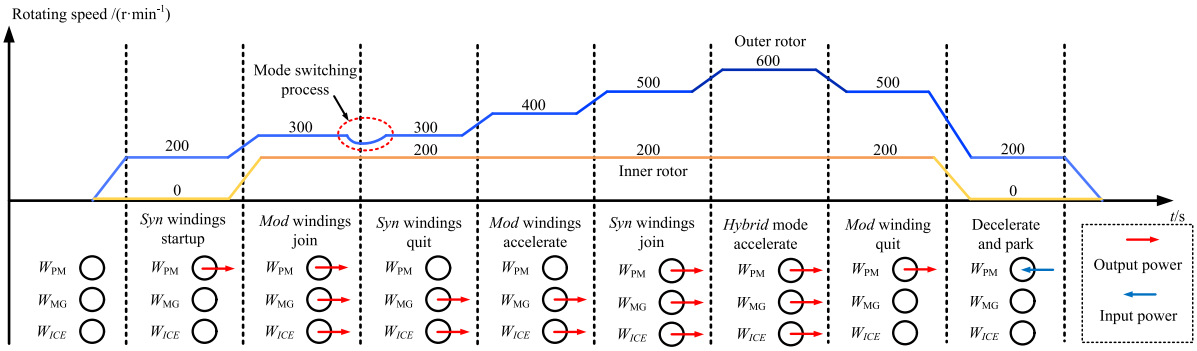

Fig. 21. Driving cycle for a typical hybrid transportation that adopts the CCPDRM.

Based on the equivalent driving cycle, the tested dynamic mode-switching process waveforms are illustrated in Fig. 22, where the phase-current, q-axis current waveforms of the modulated and synchronous windings, together with the rotating speed and torque waveforms of the outer rotor, are plotted. For all the dynamic processes, the resistive torque of the magnetic brake that is connected to the outer rotor is set as 15 N·m. It can be observed that between different mode-switching processes, the rotating speed of the outer rotor can change smoothly without overshoot, proving the CCPDRM has a good dynamic performance.

As for the systematic efficiency, two efficiency maps of the simulated and tested results are provided for comparison, as shown in Fig. 23. The torque and efficiency of the typical

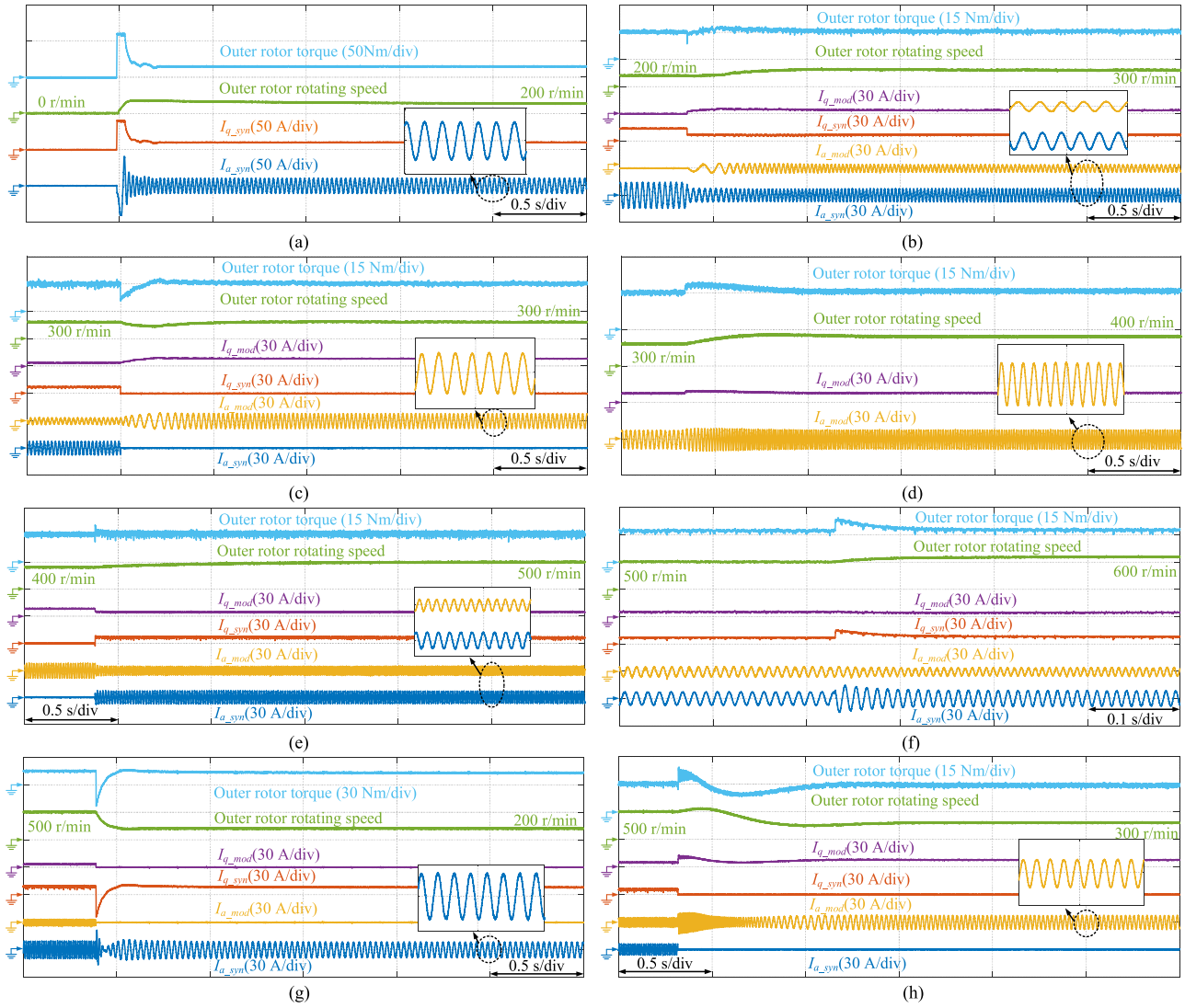

Fig. 22. Dynamic waveforms based on driving cycle in Fig. 20. (a) Synchronous winding work alone, outer rotor accelerates from 0 to 200 r/min. (b) Modulated windings joins, outer rotor accelerates from 200 to 300 r/min, with inner rotor maintaining 200 r/min. (c) Synchronous windings quits operation, outer rotor maintains 300 r/min, and inner rotor maintains 200 r/min. (d) Modulated windings works alone, outer rotor accelerates from 300 to 400 r/min, with inner rotor maintaining 200 r/min. (e) Synchronous winding joins (hybrid mode), outer rotor accelerates from 400 to 500 r/min, with inner rotor maintaining 200 r/min. (f) Both modulated and synchronous windings work, outer rotor accelerates from 500 to 600 r/min, with inner rotor maintaining 200 r/min. (g) Modulated windings quits operation, outer rotor decelerates from 500 to 200 r/min, with inner rotor maintaining 200 r/min. (h) Synchronous windings quits operation, outer rotor decelerates from 500 to 300 r/min, with inner rotor maintaining 200 r/min.

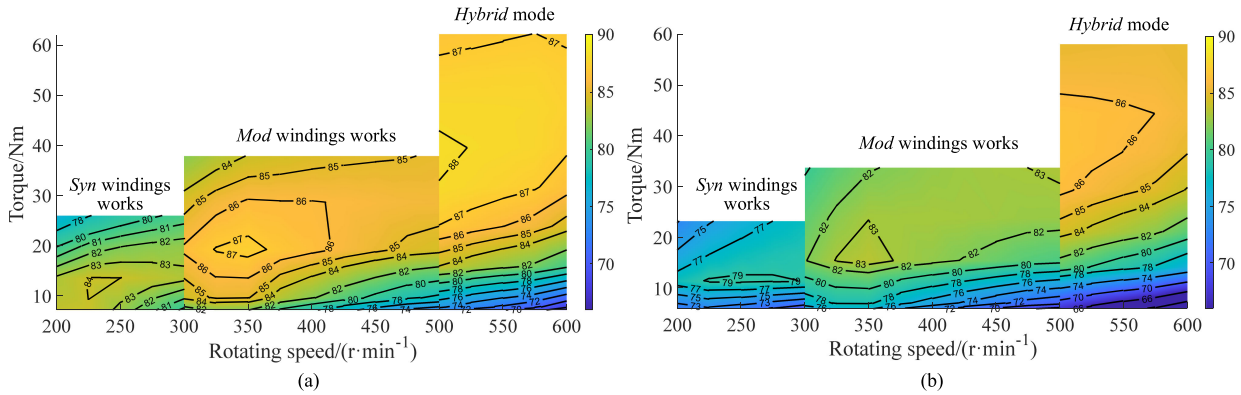

Fig. 23. Efficiency map comparisons of the proposed CCPDRM. (a) Simulated result. (b) Experimental result.

TABLE V
ON-LOAD PERFORMANCE VALIDATION OF THE CCPDRM IN THE EQUIVALENT DRIVING CYCLE

Mode	Ω_{in} / (r·min^{-1})	Ω_{out} / (r·min^{-1})	*Syn* windings Current density (A·mm^{-1})	*Mod* windings Current density (A·mm^{-1})	Outer rotor torque/(Nm)		Efficiency/%	
					FEA	Test	FEA	Test
			2	0	13.5	11.4	83.2	78.0
Syn windings works	0	200	3	0	19.9	16.7	80.0	75.3
			4	0	26.0	23.2	76.1	72.9
			0	2	19.1	15.4	86.2	82.4
Mod windings works	200	400	0	3	28.5	23.8	86.0	83.0
			0	4	37.7	33.7	84.5	82.5
			2	2	31.7	29.2	88.0	85.3
Hybrid mode	200	500	3	3	47.2	44.3	87.9	85.9
			4	4	62.0	57.9	86.6	84.7

operating modes are given in Table V. The tested efficiency is about 3%–5% lower than that in FEA. However, the discrepancy decreases as the rotating speed increases. There are two reasons for the discrepancy between simulated and tested results. First, the extra iron loss caused by pulsewidth modulation is not considered in simulation. Second, the stray loss in experiment is larger than that in the simulated result.

Since the CCPDRM can be regarded as the combination of the planetary gear, traction motor, and generator in the HPS with conventional mechanical structure, the integrated efficiency of three components should be compared with that of CCPDRM. The efficiency of a good planetary gearbox is around 97%, but it will decrease to 93% at high speed; a typical PMSM has an efficiency around 97% and 70% when serving as a generator. Thus, the overall efficiency of the mechanical system is around 80%–95%, which is a bit higher than that of CCPDRM. Indeed, the proposed CCPDRM is a little inferior to its mechanical counterpart regarding the efficiency, but it has several distinct advantages in other aspects. First, the CCPDRM utilizes the magnetic-gearing effect, so it has self-protection nature, thus preventing it from breaking down in extreme working conditions. Second, the CCPDRM eliminates the mechanical gearbox, so the physical contact between two rotating components is eliminated, leading to lower noise, smaller vibration, and longer service life. Third, the CCPDRM serves as the integration of the planetary gear, traction motor, and generator in its mechanical counterpart, leading to a more compact structure and a higher utility rate of space.

VI. CONCLUSION

In this article, a novel CDRM with a consequent-pole structure is proposed. By extending the winding factor theory of conventional electric machines to CCPDRMs, the structure and the winding scheme requirement are established. CCPDRMs can be regarded as the combination of a PMSM and an MGM, and it has a more compact structure compared with those existing MGMs. The variation relations between the torque density, PM volumetric density, and various geometrical parameters in CCPDRMs are elucidated by adopting a parameter sweep method. The electromagnetic performances of the optimized CCPDRM are compared with that of an optimized CBDRM. Although the torque density of CBDRMs is just a bit higher than that of CBDRMs, its PM volumetric density for the MGM component is almost double that in CBDRMs, proving that CCPDRMs greatly improve the PM utilization factor. Additionally, the PM demagnetization risk for CCPDRMs is lower than that for CBDRMs. This quantitative comparison between the CCPDRMs and CBDRMs proves that the consequent-pole structure is preferable for CDRMs. Finally, a CCPDRM prototype that adopts the optimal design parameters is manufactured, and the experimental results coincide well with that of FEA. Both simulation and experimental results indicate that CCPDRMs have excellent performances in various working modes. Furthermore, a whole driving cycle is tested to evaluate the dynamic mode-switching characteristic of CCPDRMs and proving that CCPDRMs have a good dynamic performance. In summary, the proposed CCPDRMs can serve as a potential competitive candidate for the eCVT in HPSs.

REFERENCES

[1] M. Yilmaz and P. T. Krein, "Review of battery charger topologies, charging power levels, and infrastructure for plug-in electric and hybrid vehicles," *IEEE Trans. Power Electron.*, vol. 28, no. 5, pp. 2151–2169, May 2013.

[2] G. Di Ilio, P. Di Giorgio, L. Tribioli, G. Bella, and E. Jannelli, "Preliminary design of a fuel cell/battery hybrid powertrain for a heavy-duty yard truck for port logistics," *Energy Convers. Manage.*, vol. 243, 2021, Art. no. 114423.

[3] D. Alexander, "Hybrid electric drive for naval combatants," *Proc. IEEE*, vol. 103, no. 12, pp. 2267–2275, Dec. 2015.

[4] F. Mauro, U. l. Monaca, C. Nasso, and V. Bucci, "An hybrid-electric solution for station-keeping and propulsion of a small coastal research vessel," in *Proc. Int. Symp. Power Electron., Elect. Drives, Autom. Motion*, 2018, pp. 607–612.

[5] M. Voskuijl, J. van Bogaert, and A. G. Rao, "Analysis and design of hybrid electric regional turboprop aircraft," *CEAS Aeronaut. J.*, vol. 9, no. 1, pp. 15–25, Mar. 2018.

[6] C. Pornet and A. T. Isikveren, "Conceptual design of hybrid-electric transport aircraft," *Prog. Aerosp. Sci.*, vol. 79, pp. 114–135, Nov. 2015.

[7] M. Gokasan, S. Bogosyan, and D. J. Goering, "Sliding mode based powertrain control for efficiency improvement in series hybrid-electric vehicles," *IEEE Trans. Power Electron.*, vol. 21, no. 3, pp. 779–790, May 2006.

[8] J. M. Miller, "Hybrid electric vehicle propulsion system architectures of the e-CVT type," *IEEE Trans. Power Electron.*, vol. 21, no. 3, pp. 756–767, May 2006.

[9] L. Sun, M. Cheng, and H. Jia, "Analysis of a novel magnetic-geared dual-rotor motor with complementary structure," *IEEE Trans. Ind. Electron.,* vol. 62, no. 11, pp. 6737–6747, May 2015.

[10] M. Wang, C. Tong, Z. Song, J. Liu, and P. Zheng, "Performance analysis of an axial magnetic-field-modulated brushless double-rotor machine for hybrid electric vehicles," *IEEE Trans. Ind. Electron.,* vol. 66, no. 1, pp. 806–817, Jun. 2018.

[11] J. Bai, P. Zheng, C. Tong, Z. Song, and Q. Zhao, "Characteristic analysis and verification of the magnetic-field-modulated brushless double-rotor machine," *IEEE Trans. Ind. Electron.,* vol. 62, no. 7, pp. 4023–4033, Jul. 2015.
[12] Y. Liu, S. Niu, and W. Fu, "Design of an electrical continuously variable transmission based wind energy conversion system," *IEEE Trans. Ind. Electron.,* vol. 63, no. 11, pp. 6745–6755, Jul. 2016.
[13] X. Ren, D. Li, R. Qu, W. Kong, X. Han, and T. Pei, "Analysis of spoke-type brushless dual-electrical-port dual-mechanical-port machine with decoupled windings," *IEEE Trans. Ind. Electron.,* vol. 66, no. 8, pp. 6128–6140, Aug. 2019.
[14] Z. Liang, X. Ren, D. Li, R. Qu, and X. Han, "Analysis of a spoke-array brushless dual-electrical-port dual-mechanical-port machine with reluctance rotor," *IEEE Trans. Ind. Electron.,* vol. 68, no. 4, pp. 2999–3011, Apr. 2021.
[15] H. Zhao, C. Liu, Z. Song, and W. Wang, "Analytical modelling of a double-rotor multi-winding machine for hybrid aircraft propulsion," *IEEE Trans. Transp. Electrific.,* vol. 6, no. 4, pp. 1537–1550, May 2020.
[16] X. Ren, D. Li, R. Qu, Z. Liang, and X. Han, "A brushless dual-electrical-port dual-mechanical-port machine with integrated winding configuration," *IEEE Trans. Ind. Electron.,* vol. 68, no. 4, pp. 1537–1550, Mar. 2020.
[17] M. Cheng, P. Han, and W. Hua, "General airgap field modulation theory for electrical machines," *IEEE Trans. Ind. Electron.,* vol. 64, no. 8, pp. 6063–6074, Mar. 2017.
[18] H. Zhao, C. Liu, Z. Song, S. Liu, and T. Lubin, "An analytical model for magnetic-geared double-rotor machines and its dq axis determination," *IET Electr. Power Appl.*, vol. 14, no. 2, pp. 175–183, Sep. 2019.
[19] Z. Zhu and Y. Liu, "Analysis of air-gap field modulation and magnetic gearing effect in fractional-slot concentrated-winding permanent-magnet synchronous machines," *IEEE Trans. Ind. Electron.,* vol. 65, no. 5, pp. 3688–3698, Oct. 2017.
[20] R. Krishnan, *Permanent Magnet Synchronous and Brushless DC Motor Drives*, 1st ed. Boca Raton, FL, USA: CRC Press, 2017.
[21] S. J. Farlow, *Partial Differential Equations for Scientists and Engineers*, 1st ed. New York, NY, USA: Courier Corporation, 1993.
[22] N. Bianchi, S. Bolognani, M. D. Pre, and G. Grezzani, "Design considerations for fractional-slot winding configurations of synchronous machines," *IEEE Trans. Ind. Appl.,* vol. 42, no. 4, pp. 997–1006, Jul. 2006.
[23] J. Bai, J. Liu, P. Zheng, and C. Tong, "Design and analysis of a magnetic-field modulated brushless double-rotor machine—Part I: Pole pair combination of stator, PM rotor and magnetic blocks," *IEEE Trans. Ind. Electron.,* vol. 66, no. 4, pp. 2540–2549, Jun. 2018.
[24] X. Han *et al.*, "Flexible energy conversion control strategy for brushless dual-mechanical-port dual-electrical-port machine in hybrid electrical vehicles," *IEEE Trans. Power Electron.,* vol. 34, no. 4, pp. 3910–3920, Jul. 2018.
[25] I. Stamenkovic, N. Milivojevic, N. Schofield, M. Krishnamurthy, and A. Emadi, "Design, analysis, and optimization of ironless stator permanent magnet machines," *IEEE Trans. Power Electron.*, vol. 28, no. 5, pp. 2527–2538, May 2013.
[26] F. Meier, "Permanent-magnet synchronous machines with non-overlapping concentrated windings for low-speed direct-drive applications," Ph.D. dissertation, School Elect. Eng., KTH, Stockholm, Sweden, 2008.
[27] R. Wrobel and P. H. Mellor, "Design considerations of a direct drive brushless machine with concentrated windings," *IEEE Trans. Energy Convers.,* vol. 23, no. 1, pp. 1–8, Feb. 2008.
[28] G. Pellegrino, A. Vagati, B. Boazzo, and P. Guglielmi, "Comparison of induction and PM synchronous motor drives for EV application including design examples," *IEEE Trans. Ind. Appl.,* vol. 48, no. 6, pp. 2322–2332, Nov. 2012.
[29] Z. Song, C. Liu, and H. Zhao, "Investigation on magnetic force of a flux-modulated double-rotor permanent magnet synchronous machine for hybrid electric vehicle," *IEEE Trans. Transp. Electrific.*, vol. 5, no. 4, pp. 1383–1394, Dec. 2019.
[30] JFE Steel Cooperation, "Electrical steel sheets JFE G-Core, JFE N-Core," 2021. [Online]. Available: https://www.jfe-steel.co.jp/en/products/electrical/catalog/f1e-001.pdf
[31] X. Luo and S. Niu, "A novel contra-rotating power split transmission system for wind power generation and its dual MPPT control strategy," *IEEE Trans. Power Electron.*, vol. 32, no. 9, pp. 6924–6935, Sep. 2017.
[32] J. Bai, J. Liu, G. Liu, Y. Liu, and P. Zheng, "Investigation of the power factor of magnetic-field modulated brushless double-rotor machine," *IEEE Trans. Power Electron.*, vol. 36, no. 1, pp. 423–432, Jan. 2021.
[33] A. F. Pacheco, M. E. Martins, and H. Zhao, "New European drive cycle (NEDC) simulation of a passenger car with a HCCI engine: Emissions and fuel consumption results," *Fuel*, vol. 111, pp. 733–739, Sep. 2013.

Hang Zhao (Student mmeber, IEEE) received the B.Eng. and M.Eng. degrees from the Huazhong University of Science and Technology, Wuhan, China, in 2015 and 2017, respectively, and the Ph.D. degree from the City University of Hong Kong, Hong Kong, in 2021, all in electrical engineering.

He is currently a Research Scientist with the University of Hong Kong, Hong Kong. His research interests include the design, analytical solution, and control of advanced electric machines.

Chunhua Liu (Senior Member, IEEE) received the B.Eng. and M.Eng. degrees in automatic control from the Beijing Institute of Technology, Beijing, China, in 2002 and 2005, respectively, and the Ph.D. degree in electrical and electronic engineering from the University of Hong Kong, Hong Kong, in 2009.

He currently serves as an Associate Professor of electrical and electronic engineering with the School of Energy and Environment, City University of Hong Kong, Hong Kong, China. In his areas of research interest, he has authored or coauthored more than 250 refereed papers. His research interests include electric machines and drives, electric vehicles and aircrafts, electric robotics and ships, renewables and microgrids, power electronics, and wireless power transfer.

Dr. Liu is currently an Associate Editor for the IEEE TRANSACTION ON INDUSTRIAL ELECTRONICS, *Open Journal of the Industrial Electronics Society, and IEEE Chinese Journal of Electrical Engineering* Editor for the IEEE TRANSACTIONS ON VEHICULAR TECHNOLOGY, IEEE TRANSACTIONS ON ENERGY CONVERSION, *IEEE Power Engineering Letters*, *Energies*, and IEEE TRANSACTIONS ON MAGNETICS Conference, and Subject Editor for *IET – Renewable Power Generation*, In addition, he is the Chair and Founder for both Hong Kong Chapter, IEEE Vehicular Technology Society, and Hong Kong and Guangzhou Joint Chapter, IEEE Industrial Electronics Society, respectively.

Zaixin Song (Student Member, IEEE) received the B.Eng. and M.Eng. degrees in electrical engineering and automation from the Harbin Institute of Technology, Harbin, China, in 2016 and 2018, respectively. He is currently working toward the Ph.D. degree in electrical and electronic engineering from the City University of Hong Kong, Hong Kong, China.

He has been working on electric machine for years. His research interests include the design, analysis, and optimization of emerging electric machines, UAV propulsion motors, and multi-physics modeling and simulation.

Senyi Liu (Student Member, IEEE) received the B.Eng. and M.Eng. degrees in vehicle engineering from Tongji University, Shanghai, China, in 2015 and 2018, respectively. He is currently working toward the Ph.D. degree in electrical and electronic engineering from the City University of Hong Kong, Hong Kong, China.

His main research interests include advanced control of motor drive systems, electric servo systems, and wireless power transmission.